ELSEVIER

International Journal of Mass Spectrometry 192 (1999) 225–243

International Journal of Mass Spectrometry

Recombination of cooled highly charged ions with low-energy electrons

Reinhold Schuch[a,*], Weiyong Zong[a], N.R. Badnell[b]

[a]*Department of Atomic Physics, Stockholm University, S-104 05 Stockholm, Sweden*
[b]*Department of Physics and Applied Physics, University of Strathclyde, Glasgow G4 0NG, UK*

Received 17 May 1999; accepted 11 June 1999

Abstract

Recent studies of recombination between free electrons and highly charged ions using the electron cooler of the "CRYRING" heavy-ion storage ring facility are reviewed. With bare ions, i.e. D^+, He^{++}, N^{7+}, Ne^{10+}, and Si^{14+} we find a strong and puzzling deviation from radiative recombination theory. Examples of dielectronic resonances above the first ionization threshold are shown, measured with a resolution in the order of 10^{-2} eV with highly charged Li-like ions stored at around 10 MeV/u kinetic energy in the ring. We discuss some issues of the stabilization of the outer electron in the Rydberg series of the doubly excited Ne^{6+} and Ar^{14+} formed in a dielectronic resonance. (Int J Mass Spectrom 192 (1999) 225–243)

Keywords: Recombination; Cooled highly charged ions; Low-energy electrons

1. Introduction

The experimental techniques for studying electron–ion collision processes have, in the last 15 years, gone through a rapid development. In the beginning of the 1980s it was still barely possible to observe most of the possible electron–ion reactions in the laboratory. Experiments started in different laboratories with conventional merged beams or crossed beams of electrons and ions, by so called "single passage" arrangements. A revolutionary development came at the end of the 1980s with the advent of heavy-ion cooler storage rings [1,2] and electron beam ion traps [3]. These devices allow investigations of reactions between electrons and ions in almost any charge state with high resolution, signal-to-background ratio, and luminosity. Primarily radiative recombination, dielectronic recombination, laser induced recombination, and dissociative recombination [1,4] were studied. Some work on electron impact excitation and ionization is done as well.

The reasons that electron-beam ion traps (EBIT) and cooler-storage ring facilities offer unique properties for the study of electron–ion reactions are manifold: In these devices, ions can be accumulated and confined under excellent vacuum for bombardment with electrons. The devices for production of ions in EBIT and for cooling ions with electrons in a storage ring provide intense, high-quality electron beams. This results in a high luminosity with low background and excellent resolution. With an EBIT, in particular,

* Corresponding author. E-mail: schuch@msi.se

PII S1387-3806(99)00130-X

photon spectra from the electron ion reactions can be observed in high resolution. It has, additionally, the advantage of allowing high electron impact energies. Storage rings, in contrast, have their strength in low impact energies. The disadvantage of not being able to perform photon spectroscopy of recombination in storage rings at present is partly compensated by an excellent energy resolution and by the selectivity in ion charge states as well as their easy detection. Otherwise EBITs have, in comparison, compact designs with low investment and operation costs; and in many aspects of electron–ion collisions they are complementary to storage rings.

In storage rings, ions are kept rotating with high velocity (up to ~50% speed of light) within a 50–100 m circumference vacuum tube guided by magnetic fields. Storage times from seconds to several days (depending on the electronic structure of the ions and the vacuum in the ring) have been observed for high circulating ion currents ranging from μA to mA. In these machines one thus has the possibility to work with a well known number of ions (10^6–10^{10}) at well defined speed and charge state. With the capability of storing ions one can also cool them. Cooling here means making the beam monoenergetic and reducing the angular divergence and geometrical size of the beam. This gives access to enormous improvements in spectroscopy of transitions and resolution in reaction channels. Stored particles can be cooled, in general, by stochastic or resistive cooling, collisional cooling (buffer gas cooling, electron cooling, sympathetic cooling), laser cooling, and synchrotron radiation cooling. Within this review we will only describe the collisional cooling method, i.e. electron cooling, in more detail because it is, at present, practically the only and by far most powerful method for cooling heavy ions. It is also the device that is used for studies of interactions of free electrons with the stored ions, as they pass ~10^6 times per second through the electron cooler. The vacuum in the ring and the high velocity guaranties a low background from rest-gas reactions. The high velocity has the additional advantage of a kinematic expansion of the energy scale in the electron–ion center-of-mass system thus leading to a high energy resolution. A recent development of using expanded electron beams has additionally reduced the temperature distributions. The resolution of interaction energies down to 10^{-3} eV at tens of eV collision energy can now be achieved. The ability to store ions for times from a fraction of a second up to several hours could also be exploited in measurements of, e.g. lifetimes of atomic metastable states.

The evolution of experimental techniques in this research has been strongly coupled to improving methods of calculating atomic structure and reaction cross sections for recombination, excitation, and ionization and radiation effects produced in collisions between ions, electrons, and atoms. Advances in this field are motivated by the need for atomic and molecular data in plasma modeling, astrophysical and fusion plasma, interstellar clouds, and from observations and modeling of supernova reminiscence and earth atmosphere.

2. Experimental methods

Heavy ion cooler storage rings in present operation are ASTRID in Arhus [5], CRYRING in Stockholm [6], ESR at GSI Darmstadt [7], TARNII in Tokyo [8], and TSR in Heidelberg [9]. For storing heavy ions, the vacuum has to be in the low 10^{-11} mb pressure region in order to obtain an adequate beam lifetime and low background counts. One has dilute atomic or molecular gas targets (ESR and CRYRING), continuous or pulsed laser systems, and the electron cooler as central devices in heavy ion rings. At CRYRING, of the Manne Siegbahn Laboratory, Stockholm, ions from a plasmatron ion source or for high charge states (q) from an electron–beam ion source (EBIS) are injected into the storage ring. Starting at 5–50 keV x q, they can either be injected directly into the ring or after preacceleration to 300 keV/u in a radio-frequency quadrupole (RFQ). After storing the ions, they are further accelerated to $96(q/A)^2$ MeV/u maximum energy (A is the atomic or molecular weight number). The motion of ions in the ring is governed by magnetic fields that provide the confining forces on the ions—usually, a periodic structure of magnetic elements; dipole magnets provide the centripetal

force, and higher order magnetic multipole fields the focusing force for radial confinement [10]. Between the magnets there are drift lengths containing the beam injection elements, the device for acceleration, the electron cooler and targets, as well as detector installations for experiments. This structure that repeats itself periodically is called a superperiod. For example CRYRING has a (bend, focus, defocus, focus, bend, drift) superperiod, with six of such superperiods, a sixfold symmetry. After injection, the ions fill the whole aperture of the ring. Acceleration decreases the beam emittance somewhat, but it is the possibility for cooling the stored ions that makes storage rings such powerful tools for providing intense beams of low emittance and high energy definition.

2.1. Cooling of highly charged ions

The most widely used methods for ion–beam cooling are electron cooling [11] and stochastic cooling [10]. Stochastic cooling requires a long time and is thus not practical for cooling heavy ions. Electron cooling works via long-range elastic Coulomb scattering of the electrons from the ions. It was first demonstrated with protons [11], and much later for heavy ions. Here, the concern was that the beam could be lost due to large electron–ion recombination rates or heated more rapidly through strong ion–ion scattering of the highly charged ions than cooled. Another ion cooling method is laser cooling [12]. This mechanism cannot, however, be applied to highly charged ions, but instead is applied to singly charged ions with a suitable optical transition.

For electron cooling, a monoenergetic electron beam [having the same velocity as the stored ions (v_i)] is merged with them over a length of 1–2 m. A schematic view of the electron cooler installed at CRYRING [13] is shown in Fig. 1. The electrons are emitted from a hot cathode ($T \approx 1000$ K) having a radius of around 2 cm. A magnetic field with a strength B in the order of 0.02–0.05 T guides the electrons through the overlap region to the collector and prevents them from diverging. The ion beam is thus completely immersed in a constant density electron beam. Typical electron densities are on the order of $n_e \sim 10^7$ cm^{-3}. Cooling occurs by collisions with the low-temperature electrons as the ions pass through the cooler at approximately one million times per second as they circulate in the ring. Thus, at thermal equilibrium, the ion–beam energy spread will be reduced from MeV to a few eV. At CRYRING electron cooling has been applied both to atomic and molecular ions at energies between 290 keV/u (the injection energy) and 24 MeV/u. The relative momentum spread of the ion beam after cooling is usually 5–10 $\cdot$ 10^{-5} and occasionally somewhat smaller, depending on the ion density, charge, and mass (see below). With Ar^{15+}, where cooling is considerably stronger than for low charged ions, 1.6 $\cdot$ 10^{-5} was recorded. The reduction of the momentum spread during cooling is seen in the longitudinal Schottky noise spectrum [10]. Two effects are observed in the Schottky spectrum: (1) the area of the Schottky peak remains nearly constant, i.e. its width decreases with increasing signal height demonstrating directly the concentration of the particles in momentum space by cooling, and (2) the noise spectrum of the cooled beam splits into two peaks around the harmonic center frequency. This is explained by backcoupling of particle density fluctuations, via the walls of the vacuum chambers, on the following particles in the beam. In the case of cold dense beams, where the random component is suppressed, this leads to the excitation of collective modes for the particle motion: i.e. waves of density fluctuations propagate and counterpropagate in the stored beam. These waves modulate the revolution frequency and show up as a peak splitting in the longitudinal noise spectrum.

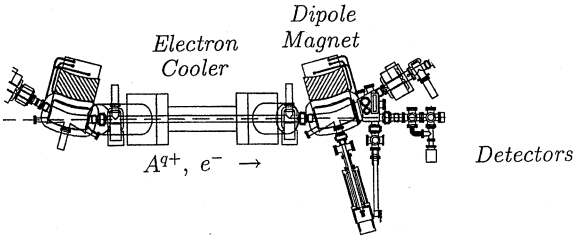

Fig. 1. The experimental setup showing the section of CRYRING with the electron cooler and the actuators for placing detectors into the ultrahigh vacuum system.

2.2. Characteristics of the electron beam

The thermal emission of the electrons at T_K = 1000 °K corresponds to an electron energy spread of $kT_K \approx 0.1$ eV. Acceleration to the energy $E_e = (m_e/2)v_{e0}^2$ reduces the longitudinal temperature by a large factor $T_{e\|} = (kT_K^2)/(4E_e)$. The effective longitudinal temperature is, due to space charge relaxation between electrons in the beam, the so-called longitudinal–longitudinal relaxation [13,14], increased to $T_{e\|} = 1.6e^2 n_e^{1/3}/(4\pi\epsilon_0)$. The electron gun in the present version of the CRYRING cooler uses a two-stage acceleration: After the first anode, the electrons go through a 25 cm long metal tube before they are accelerated to the final energy. Inside this tube, the electron density is around 10^9 cm^{-3}. Relaxation should then give $T_{e\|} = 2 \cdot 10^{-4}$ eV. At the second acceleration stage, from, e.g. 500 eV to final energy, the longitudinal energy spread becomes reduced by a factor equal to the ratio between the two energies to $T_{e\|} \leq 0.1$ meV/k. A further relaxation takes place after the second acceleration, increasing $T_{e\|}$ by an almost negligible amount. Almost all electron coolers have typical values of $T_{e\|} \sim 0.1$–1 meV/k for the longitudinal temperature. The transverse electron temperature would be $T_{e\perp} \sim 0.1$ eV/k. Recently, a big step toward lower transverse energy spread of the electron beam was achieved by an adiabatic expansion of the electron beam in the guiding magnetic field [13]. Almost all electron coolers have expanded electron beams nowadays. At TARNII and CRYRING the expansion factor is up to 100 (which can result in a decrease of $T_{e\perp}$ to 1 meV/k), TSR has expansion of up to 30, and ASTRID has expansion of up to 20.

The electron velocity distribution $f(\vec{v}_e)$ is described by a flattened Maxwellian distribution:

$$f(\vec{v}_e) = C \exp\left(-\frac{m_e}{2}\frac{v_{e\perp}^2}{kT_{e\perp}} - \frac{m_e}{2}\frac{(v_{e\|} - v_{\mathrm{rel}})^2}{kT_{e\|}} \right) \quad (1)$$

where $C^{-1} = (2\pi/m_e)^{3/2} kT_\perp (kT_\|)^{1/2}$ is a normalisation constant and v_{rel} is the average longitudinal center-of-mass velocity (see below).

2.3. Principles of electron–ion collision measurements

The cooling condition is obtained when the mean ion and electron velocities are equal to each other, which defines the electron cooling energy as $E_{\mathrm{cool}} = (m_e/m_i)E_i$. Here E_i is the energy of the stored ions, whereas m_e and m_i are the electron and projectile mass, respectively. After cooling the ion beam, the electron energy can be changed by a certain amount ΔE that results in a center-of-mass (CM) energy: $E_{\mathrm{cm}} \approx \Delta E^2/4E_e$. Small collision energies can easily be reached. For instance, if a 10 keV electron beam for cooling 19 MeV/u ions is detuned by $\Delta E = 500$ eV, the resulting collision energy is only about 6 eV. The exact relativistic expression for the mean center-of-mass energy, also called relative energy, is:

$$E_{\mathrm{rel}} = [(E_e + E_i + m_e c^2 + m_i c^2)^2 - \sqrt{(E_e^2 + 2m_e c^2 E_e} + \sqrt{E_i^2 + 2m_i c^2 E_i})^{21/2} - m_e c^2 - m_i c^2 \quad (2)$$

The energies E_e and E_i are determined by acceleration potentials and do not a priori contain beam temperatures. The center-of-mass velocity v_{cm} agrees therefore only at high detuning energies with v_{rel}; in that case $E_{\mathrm{cm}} = E_{\mathrm{rel}}$.

The recombined atoms or ions are separated from the stored ion beam in the ring by the first bending magnet after the electron cooler and detected (see Fig. 1). This is done with surface-barrier (SB) detectors, channel plates, or scintillators. Fig. 1 shows the arrangement of the manipulators used to insert the detectors in the ring vacuum. The advantage of SB detectors is that they have detection efficiency unity and reasonable good energy resolution. Channel plates and scintillators have a detection efficiency dependent on the ion charge and energy and do not have a good energy resolution; however, they do have the advantage of high irradiation thresholds. Position sensitive channel plates are useful to monitor the spatial distribution of detected atoms. In that way, valuable information on beam cooling can be acquired

and used in optimizing the alignment of electron and ion beams [15].

With detection of charge changed projectiles after a ring dipole magnet (Fig. 1), the field ionization of loosely bound electrons in the motional electric field in the ring bending magnet needs to be considered. It limits the number of detected ions to those that recombined into states with values of the principal quantum number n, smaller than some critical $n_{\max} = (6.2 \times 10^{10} q^3/\varepsilon)^{1/4}$ [16] where q is the ion charge and $\varepsilon = v_i B$ is the motional electric field strength (in units of V/m) determined by the magnetic field B and v_i. The effect of $n_{\max}$ on the measured recombination rates will be discussed in detail in Sec. 3.2.

In the experiment the electron energy is scanned around E_{cool} within selected energy intervals in the ions' rest frame. After a scanning interval of typically 1 s a one to several seconds recooling interval at cooling energy follows in order to ensure that the ion beam remains properly cooled. The duration of the recooling interval in each cycle is given by the observed beam cooling time, usually about 1–5 s.

For each recombination event detected, the cathode voltage U_{cath} and the time t related to the scanning trigger, the particle detector pulse height, stored ion number, and so on are recorded in event mode. From U_{cath} and the Schottky frequency one could obtain the parameters E_e and E_i, respectively. Deriving E_{cm} from such values lacks, however, a high accuracy. Different ways to get E_{cm} with high accuracy, which were developed in experiments at CRYRING, are described below.

2.4. Absolute rate coefficients as function of energy

The recombination rate coefficient α_{exp} derived from first principles for a number of stored ions N^i reacting with an electron target is:

$$\alpha_{\text{exp}}(t) = \gamma^2 \frac{N_t^{\text{corr}}/\delta t}{n_e N^i (\ell/L)} \tag{3}$$

where γ is the Lorentz factor and L stands for the ring circumference. The detected ion rate per time unit δt at time t of the scan ($N_t^{\text{corr}}/\delta t$) is corrected for the electron capture background. This background amounts to a few percent at a pressure of 10^{-11} Torr. The number of circulating ions is calculated from the relation $N^i = \mathcal{I}/(e f_s)$. One gets the ion circulation frequency f_s from the Schottky noise detector and the current $\mathcal{I}$ of the ion beam is measured with the current transformer. In CRYRING, e.g. the ions are merged with electrons over a length of 1 m. The effective length of the interaction in recombination experiments is $\ell = 0.8 + -0.06$ m. This is determined in the following way: The deflection of the electron beam at both ends of the beam overlap region in the electron cooler induces a dependence of the relative energy upon the position in the field fringe regions. Considering the mapping of the magnetic field [17] in the electron cooler, we have presently arrived at the above estimate for the effective cooler length ℓ. For the ion orbit length L one can take here the nominal length (from the ring construction) of 51.6 m. The values of α_{exp} therefore have a systematic error of around 10%, originating mainly from the uncertainty in the ion current.

In Fig. 2 the scheme of data taken is shown for the case of Ne^{7+} [18] (middle); the detuning of the cathode voltage from transformed cooling is shown. The lower part of this figure displays the corresponding CM energies. At the top of Fig. 2 four spectra are displayed—two where the electrons moved faster and two where they moved slower than the ions. One does not record the recombined ion spectrum as a function of cathode voltage but instead in a histogram as a function of time ("time spectrum") (see Fig. 2). The "time spectrum" is superior to the former for the following reasons: First, the time signal is digitally generated, which is free of pickup noise, and the total number of channels in a time spectrum is independent of the energy scan range. This allows one to preserve the high resolution gained from the low electron temperature. Second, the time spectra contain information revealing the variation of the ion energy during the scan of the cathode voltage, which is used in the drag force correction (see below). Finally, it is convenient to derive the rate from it because each channel has equal time length.

The time spectra are converted into energy spectra

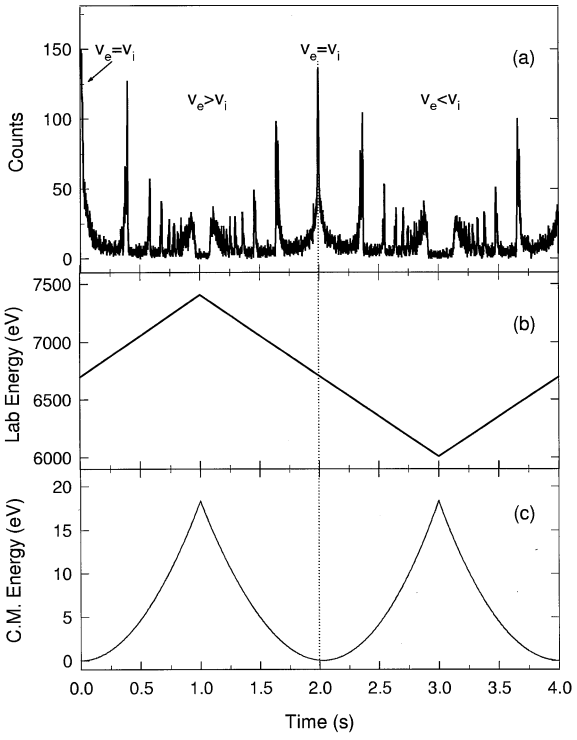

Fig. 2. Scans of the recombination rates for the stored lithium-like Ne ions. Top: counts of recombined ions; two spectra where the electrons moved faster and two where they move slower then the ions. Note that the high peak at the center, which is from the nonresonant recombinations, defines precisely the time and electron energy at which the electron velocity equals the ion velocity. Middle: variation of cathode voltage. Bottom: CM energy as a function of scanning time.

by converting each time channel into the corresponding cathode voltage, which is derived by averaging the recorded cathode voltages over all individual events associated with that time channel. Because of the distorted response of the cathode to its power supply, an inadequate error will be introduced when deriving these energy values simply from the function generator that drives the power supply. The energy spectra derived from the time spectrum are checked with the energy spectra obtained directly from the data by comparing the corresponding resonance peaks. Mismatches are found to be within one time channel, so that the extra error introduced by the conversion is negligible. The total energy error caused by the conversion from time channel to cathode voltage is estimated to be 0.4% within the energy range of 1–100 eV in the center of mass frame.

One still has to correct the electron kinetic energy for the space charge of the electron beam:

$$E_e = eU_{\text{cath}} - (1 - \zeta)I_e r_e m_e c^2/ev_{e0} \times[1 + 2\ln(r_1/r_2) - (r/r_2)^2] \quad (4)$$

where r_1 and r_2 are the radii of the beam tube and of the electron beam, respectively. The classical electron radius is denoted by r_e and r is the ion beam displacement from the electron beam axis. When the two beams are coaxial, then $r = 0$. The parameter ζ represents here the contribution of trapped ions to the space charge potential. Those ions can be produced by ionization both from the electrons as well as by the ion beam. Even if those ions are not trapped (i.e. they are "cleared" by electrodes), their steady-state density can influence the absolute energy calibration. Generally the density of the trapped ions can be a complex function of the electron energy because their creation rate is electron energy dependent and their trapping potential depends on the electron density. However, in the case where the energy scan covers only a narrow range as in this experiment, ζ can be regarded as being constant. Another source of uncertainty for the electron–ion energy scale is the above-mentioned exact position of the ion beam relative to the electron beam axis. The condition $r = 0$ is assumed in most experiments with the argument that the ion beam is only 1 mm in size after cooling and is aligned to the axis of the electron beam by minimizing the Schottky frequency.

The compensation parameter ζ can be determined, in principle, by inserting the cathode voltage U_{cath} and electron energy E_e at cooling into the above formula. The value of E_e can be determined from the ion velocity at cooling and the latter can be derived from the Schottky frequency and the length of the ion orbit L. Thus, accurate determination of the ion velocity relies on the knowledge of the orbit length. In the model used here, the orbit length and trapped ion density are interconnected. If the trapped ion density is proportional to the space charge potential that confines the ions, the value of ζ should not differ very

much for two measurements where the electron energies at cooling are equal. One can thus check the values of ζ and get an estimate of the value of L and its systematic error. For CRYRING it was found that $L = 5168.5$ cm is an adequate estimate. This value is longer than the geometrical length of the ring along its axis by about 4 cm, which can be within the possible variation of the orbit in the ring apertures. In experiments of laser-induced recombination [19] this value was checked by the well known $2p$ binding energy in hydrogen. It was found there to be higher than the geometrical length by the same amount. Typical values of ζ are found here to vary from 0.7–0.8 for $I_e = 250$–50 mA, respectively, i.e. 20–30% compensation of the space charge by trapped ions.

The very low temperature of the electron beam introduces a strong drag force on the ions at small detuning velocities. This disturbs the transformation from laboratory to CM energies. For its correction, we have calculated the change of the velocity of the ions as a function of time during the scans by numerical solution of the differential equation describing the beam acceleration due to multiple Coulomb collisions in the electron beam (for details see [20]). With the inclusion of this correction the energy scans from the laboratory system can be transformed into the center-of-mass system. The four spectra obtained from the zig-zag scans (see Fig. 2) should be identical in the CM frame. In order to check these corrections, one selects the best two pronounced peaks in the spectra in the low energy region where the drag force effect is strong. Mostly, it is found that the initial large discrepancy in energy positions among the same resonance peaks from the four different parts of the zig-zag scan is removed by the drag force correction. With these corrections for the transformation an agreement of the spectra to around 10 meV is possible. A residual energy difference between the high scans and low scans could be caused by an overall shift in relative lab energy because of an error in determining the ion beam energy at cooling. A slight shift (10^{-5}) of the ion energy compensates for the small energy differences in both measurements and reduces the residual deviation. This energy shift is well within the precision of the ion energy determination in ring experiments. With the four spectra overlapping so well, after drag force correction, it is possible to combine them to obtain better statistics. Good alignment in energy is, of course, essential for adding spectra. A mismatch of much less than the obtained resolution is conditional, in order not to obscure the energy resolution and the observed features. A systematic error in the absolute energy calibration by this method is estimated to 20 meV in scans up to $E_{\mathrm{rel}} \sim 1$ eV, and somewhat more for higher energies.

A higher accuracy in the absolute energy calibration is obtained by the following method [21,22]: One selects calibration points in the scan (usually the maxima of prominent resonance peaks in a spectrum). The corresponding cathode voltage of the cooler then needs to be recorded. This is done by setting square voltage pulses around the peak. For each step, the recombination rate is recorded in the given time window. As the energy shifts due to drag force, the changing Schottky frequency is measured in the same time window. The cathode voltage where the normalized rate has a maximum is taken as the calibration point. The cathode voltage is then set to each recorded value and the ion energy is adjusted until cooling at this new voltage is reached. Under cooling conditions, the velocity of the electron beam matches the velocity of the ion beam. Because the latter can be derived from the Schottky frequency, f_s, by $v_i = f_s L$, the velocity and the energy of the electrons can be readily deduced. It should be pointed out that the electron energy deduced in this approach is absolute—the effect of the space charge is automatically included and need not be corrected for. The electron energies of the calibration points deduced by this method are converted to the CM frame and the dielectronic recombination (DR) spectrum is calibrated by aligning the calibration points to the obtained values. The systematic error is mainly determined by an uncertainty in the ion trajectory length around the ring. It is assumed to be in the order of centimeters. The absolute energy calibration by this method is estimated to be uncertain to 5 meV in scans up to $E_{\mathrm{cm}} \sim 1$ eV, and somewhat more for higher energies, at

present. A better determination of L will reduce this error accordingly.

The energy resolution for measuring resonances with the electron cooler of a storage ring is determined by the following parameters. First, the velocity spread of the cooled ion beam is small compared to that of the electron beam. At small collision energies, the cathode temperature and the beam expansion factor set the energy resolution ΔE_{cm}. At larger collision energies the longitudinal energy spread of the electron beam gets more important:

$$\Delta E_{\mathrm{rel}} = kT_{e\perp} \ln 2 + 4\sqrt{(E_{\mathrm{rel}} kT_{e\|} \ln 2)} \tag{5}$$

Additional factors in the energy resolution are due to space-charge effects: (1) The space-charge-induced potential has a parabolic shape across the ion beam that enhances the effective longitudinal electron temperature. But one has to take into account that the cooled ion beam has a diameter (~1 mm) considerably smaller than that of the electron beam (~50 mm). (2) A misalignment between the cooled ion beam and the electron beam will enhance the effective transverse electron temperature. The energy resolution that was obtained in dielectronic recombination experiments will be discussed in Sec. 3.

3. Recombination studies between electrons and highly charged ions

Electron–ion recombination processes appear as important phenomena in astrophysical plasmas [23], the chemistry of interstellar clouds [24], and in fusion plasma [25]. In fact, dielectronic recombination was postulated to explain discrepancies in the ionization balance of the solar corona [26]. Much of the energy transport and reactions in these plasma and media occur as electrons collide with atomic and molecular ions. In such collisions, the ions can be excited or further ionized, or the electrons can recombine leading to emission of photons, excitation of ions, or dissociation of molecules. In recent years recombination studies obtained a decisive role also in fundamental atomic spectroscopy [27–31]. This is because of the new possibilities given by coolers in storage rings that allow measurements of electron-impact ionization and recombination with unprecedented resolution and luminosity. When comparing experimental and theoretical results one frequently folds the theoretical cross section or resonance strength with the electron velocity distribution:

$$\alpha(E_{\mathrm{rel}}) = \int v_{\mathrm{cm}} \sigma(v_{\mathrm{cm}})\, f(\vec{v}_e) d^3 v_e \tag{6}$$

where α is the recombination coefficient and σ is the recombination cross section for the respective process. For astrophysical and plasma applications, the recombination rate coefficient is mostly needed as a function of temperature:

$$\alpha(T) = 8\pi m_e/(2\pi m_e kT)^{3/2} \times \int (\sigma_{\mathrm{RR}} + \sigma_{\mathrm{DR}})\, E_{\mathrm{cm}} \exp(-E_{\mathrm{cm}}/kT) dE_{\mathrm{cm}} \tag{7}$$

In cases where the recombination coefficient is measured over an appropriate wide energy range, the rather uncertain theoretical values $\sigma_{\mathrm{RR}} + \sigma_{\mathrm{DR}}$ might be replaced by the experimental α_{exp}.

3.1. Recombination of bare ions

Radiative recombination (RR) is defined as the capture of a *free* electron e by an ion of charge q accompanied by the emission of a photon γ:

$$A^{q+} + e \rightarrow A^{(q-1)+}(n) + \gamma \tag{8}$$

where n is the principal quantum number. It is convenient to view this process as an inverse photoionization applying the principle of detailed balance. The prototype RR process with completely stripped projectiles represents a genuine three-body problem because simultaneous conservation of energy momentum strictly precludes formation of the hydrogenlike atomic system without the presence of an external particle or field. This additional particle in RR is the photon γ that can carry off the excess energy. How-

ever, the same atomic system $A^{(q-1)+}(n)$ can also be formed if two electrons initially strike the projectile, where one of them is captured and the other remains free, carrying away the excess energy:

$$A^{q+} + e + e \rightarrow A^{(q-1)+}(n) + e \tag{9}$$

This is the so called three-body recombination that can alternatively be considered an inverse to the process of electron impact ionization of $A^{(q-1)+}(n)$.

In the case of RR one can give simplified explicit expressions for cross sections. The most practical way to accurately compute the recombination rate α_n^{RR} is accomplished through the use of the semiclassical Kramers cross section [32] corrected by the Gaunt factor $g(E)$ [33,34] in Eq. (9), i.e.

$$\sigma_n(E_{\mathrm{cm}}) = g(E_{\mathrm{cm}}) \cdot \frac{32\pi}{3\sqrt{3}} \alpha^3 a_0^2 \frac{Z^4 \mathcal{R}^2}{nE_{\mathrm{cm}}(n^2 E_{\mathrm{cm}} + Z^2 \mathcal{R})} \tag{10}$$

where $32\pi/(3\sqrt{3})\alpha^3 a_0^2 = 2.105 \times 10^{-22}$ cm^2, Z is the nuclear charge and $\mathcal{R}$ denotes the Rydberg constant. The Gaunt factor above is expressed as $g(E_{\mathrm{cm}}) = 1 - A - B - 2AB$, where $A = 0.17285\ (u-1)[n(u+1)]^{-2/3}$, $B = 0.04959\ (u^2 + 4u/3 + 1)\ [n(u+1)]^{-4/3}$, and $u = n^2 E_{\mathrm{cm}}/Z^2\mathcal{R}$. The correction $1 + A - B$ was first introduced in the above form by Burgess [33], whereas the higher-order Gaunt factor $1 + A - B - 2AB$ was proposed by Aaron et al. [34]. The quantum-mechanical first-order perturbation theory [35] for the same problem was originally implemented by Stobbe [36]. The very simple expression (above) is found to be in remarkable agreement with the numerical calculations using the Stobbe theory. We found that, for zero relative energy (cooling conditions), the radiative recombination rates $\alpha_n^{\mathrm{RR}}(E_{\mathrm{rel}})$ calculated from the approximate closed form expression obtained in [37] agree with the most accurately calculated values within a few percent.

Earlier studies on radiative recombination were done by Andersen et al. [38] as well as by Andersen and Bolko [39] in single-pass experiments. They measured the rate coefficient for recombination of He^{2+}, C^{6+}, and F^{9+} ions with free electrons and found good overall agreement with the prediction for radiative recombination using the Stobbe theory [36]. For highly charged partially stripped projectiles C^{5+}, O^{7+}, F^{8+}, Si^{6+}, and Si^{11+} investigated in [40–42] the Gaunt factor corrected Kramers [32] approximation is successful only when a judicious choice of the effective nuclear charge is made.

In experiments made at the "TSR" storage ring on electron–ion recombination for several bare and nonbare ions [43] it was found that the recombination rates are systematically 1.2–1.6 higher than predicted by RR. In particular, these experiments found that the recombination rate measured for C^{6+} ions did not agree with theoretical RR rates, contrary to the conclusion made by Andersen and Bolko [38,39] for the same system. Similar observations were made by Müller et al. [44] and Frank et al. [45] in experiments with a high density ($\sim 10^{10}$ cm^{-3}) electron beam merged with a beam of U^{28+} and, respectively, Au^{25+} and Ar^{15+} ions. They found that the Kramers–Gaunt approach, including a choice of an effective nuclear charge, systematically yields a factor of 4–50 smaller results than the experimental data. These authors suggested that the observed discrepancies could possibly be explained by taking into account the so-called collisional-radiative recombination [46] that is expected to play a more important role at higher electron densities. Later it was found [47] that a contribution by DR resonances near threshold are able to dramatically enhance recombination rates at low energies.

At CRYRING we performed a series of recombination studies for bare ions (where DR is excluded and the nuclear charge is defined), i.e. for D^+, He^{2+}, N^{7+}, Ne^{10+}, and Si^{14+} [48]. Fig. 3 shows the measured rate coefficients in the energy region below 1 eV, and the corresponding theoretical radiative recombination predictions calculated according to [34,36], and convoluted with the electron velocity distribution characterized by $T_\perp = 10$ meV/k and $T_\parallel = 0.12$ meV/k (full curves). On an energy scale below 1 meV one should keep in mind that E represents the energy difference between electron and ion beams.

The measured D^+ rates agree well with the calculated RR curve, as observed before [49–51]. All the

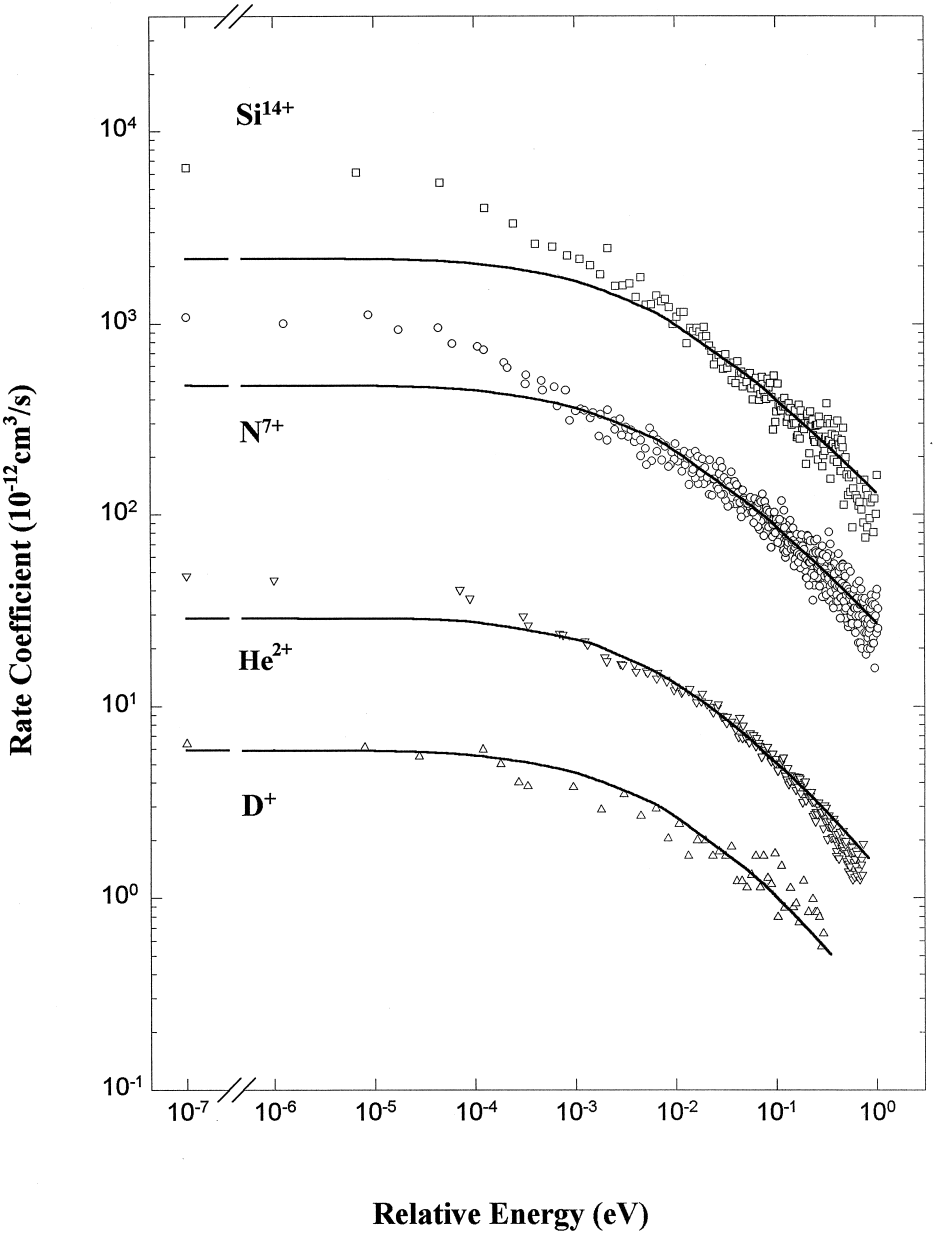

Fig. 3. Measured recombination rates $\alpha_{exp}(E)$ for D^+, He^{2+}, N^{7+}, and Si^{14+} and the corresponding theoretical radiative recombination predictions calculated using the Kramers formula with Gaunt correction, and convoluted with the electron velocity distribution characterized by $T_\perp = 10$ meV/k and $T_\parallel = 0.12$ meV/k (solid curves).

measured rate coefficients in the figure are absolute except that for Si^{14+}. This one is normalized (because of the small number of stored ions) to the high energy part (>10 meV) where all data agrees with the RR theory. For all the heavier ions increasing deviations from the RR theory are found at low relative energy. In the regime of energies below 10^{-3} eV, the average center of mass energies of the electron–ion systems

should be constant and close to $kT_\perp$. It is therefore striking that the "excess" recombination rates change strongly for variations of E much below $kT_\perp$. This important finding cannot be explained without assuming a modification of the electron velocity distribution such that the transverse motion of the electrons is "frozen" regarding the process that causes this enhancement. An argument for the latter may be found by considering the guiding solenoidal field of 0.03 T in the cooler that forces the electrons onto cyclotron orbits with a mean radius of about 8 μm, less than the average distance between electrons of 23 μm. The transverse motion could thus be confined in these orbits and the electrons collide with each other mainly via the longitudinal direction, resulting in the observed characteristics of the enhanced rates at such small E. Under the static conditions of cooling, the mean longitudinal velocities of electrons and ions are equal and the values of the rates are found to correspond to those at E below 10^{-4} eV.

One of the proposed mechanisms for the enhanced rates of bare ions is collisional recombination [46] which is a general form of three-body recombination. Very high n states are predominantly populated by collisional recombination. This can be understood by considering collisional recombination as the time reverse of electron impact ionization, and by remembering that this cross section decreases very rapidly with the binding energy of the electron. With electron temperatures in the range of fractions of eV, the electron impact ionization cross section has its maximum at around this value of the binding energy. The recombined electrons in such highly excited states can again be ionized by collisions with free electrons or stabilized collisionally or radiatively to lower n. These effects have been investigated by field ionization of Rydberg states populated in the cooler [52] and by laser induced recombination [19], without clear evidences. Because at least two electrons are involved in TBR it should be characterized by a quadratic dependence of the rate on the electron density [53]. Such a dependence has been investigated with Ne^{10+} over a factor of 5 in n_e. Even though the measured rate coefficient of Ne^{10+} is enhanced by a factor of 3 at zero relative energy, it is constant as a function of n_e within the experimental uncertainty [53]. This result does not necessarily contradict TBR as the electron beam temperatures vary with density and TBR is also sensitive to this parameter [54]. It must, however, be emphasized that no currently available theoretical model properly describes all channels and balances of recombination, radiative stabilization, collisional deexcitation, and reionization in a cold, tenuous, magnetized plasma.

The comparisons with theoretical recombination rates are biased by uncertainties in relevant experimental parameters, namely the electron beam temperatures $kT_{\parallel,\perp}$ and a critical $n_{\max}$ for the field ionization effect. The transverse electron beam temperature $kT_\perp$, which dominates the calculated rates for a flattened electron beam, is known within about 25% from electron cooling force measurements [13], from fitting dielectronic recombination resonances near threshold (see below) and the observed falloff of the laser induced recombination gain [19]. The values derived from these different methods are quite consistent with each other and are in most of the cases above the nominal transverse temperature. This discrepancy could probably be explained by influences of the regions entering and exiting the electron beam and by possible misalignments of electron and ion beam. A higher transverse temperature will in any case reduce the theoretical recombination rate at low energies.

These effects are illustrated in Fig. 4 with the example for the recombination rate close to zero relative energy measured with Ne^{7+}. The lines in the figure are convolutions of RR cross sections with different electron temperatures $T_\perp$. The RR cross sections are calculated by using the Kramers formula with Gaunt correction and an appropriate effective charge of 7.02, derived from corresponding quantum defect [55]. RR into $n = 1$ is excluded. The validity of the cross section estimation is checked and confirmed by the good agreement with the result of a distorted-wave calculation. There are no dielectronic recombination resonances expected below 1 eV. In the same spectrum these resonances are used to obtain an estimate of $T_\perp$ (see above). As shown in the figure, the shape of the rate coefficient curve varies with the

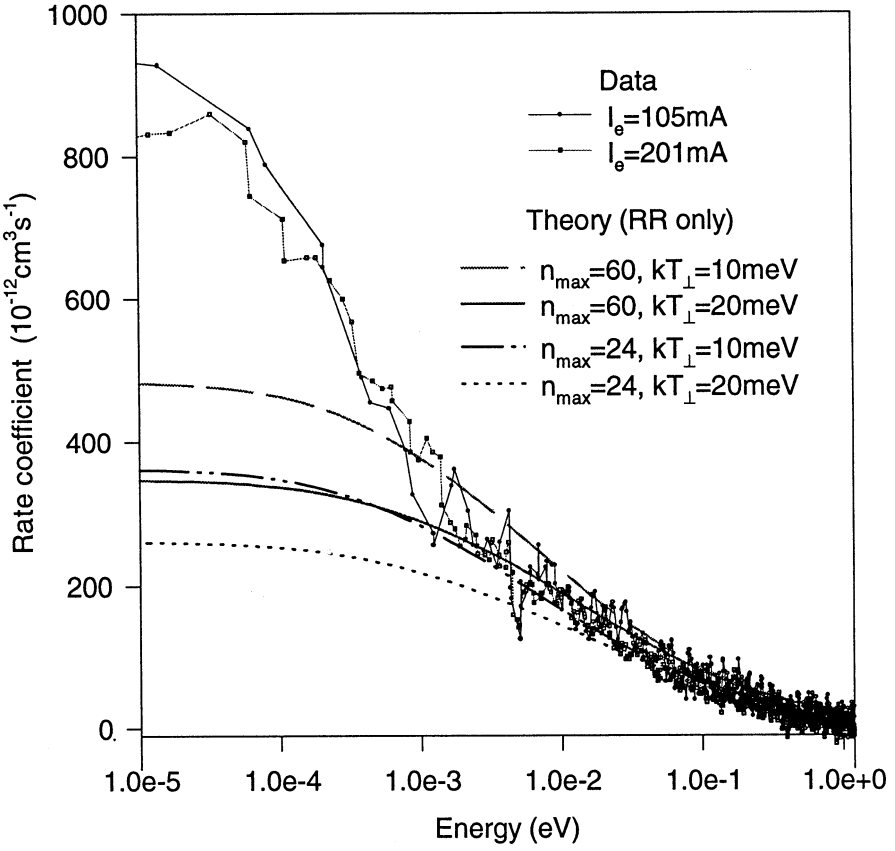

Fig. 4. Comparison of the measured nonresonant recombination rate with Ne^{7+} to the expected radiative recombination rate in the low energy region. The RR cross sections are calculated using the Kramers formula with Gaunt correction, summed up to $n_{max} = 24$ and 60, and folded with 10 meV and 20 meV transverse temperatures.

highest n states being included and with the electron temperatures used for convolution. However, even the curve including Rydberg states up to $n = 60$ and folded with $kT_{\perp} = 10$ meV, which should give an upper limit for the RR rate, shows a large discrepancy at low energies. The experimental rate coefficient starts to rise at around 10^{-3} eV as above for bare ions, i.e. below the transverse temperature, and is found by approximately a factor of 2 higher than the RR contribution at the zero energy limit. It should be noted that reasonable agreement could be obtained if the transverse temperature of the electrons is as low as ~2 meV. This low temperature contradicts, however, the temperature that fits the resonances in the same spectrum. In this experiment, data taken with different electron densities ($I_e = 105$ mA and $I_e = 201$ mA), show the same amount of enhancement. No indication of an electron density dependence was thus found in accord with the results of [53].

3.2. Recombination of lithium-like ions

With nonbare ions a free electron can be captured by the bound electron taking up energy and being excited. This doubly excited state ($d = n_1, l_1; n_2, l_2$) may stabilize by emitting photons:

$$A^{q+} + e \rightarrow A^{(q-1)+}(n_1, l_1; n_2, l_2) + \gamma \qquad (11)$$

Due to energy conservation, this recombination occurs as a resonance when the electron velocity is changed relative to the ion velocity. An unprece-

dented resolution of these resonances was found in several experiments with ions from He^+ up to Au^{76+} [27,29]. Measurements of these resonances can serve as testing grounds [20,28–31] for highly accurate calculations of energy levels, autoionization, and radiative rates in a few electron ions that require, besides the binding to the nucleus, a proper relativistic treatment of the interactions between all the electrons.

For the case of isolated resonances in the intermediate doubly excited state with energy E_d, the DR cross section as a function of the center of mass energy can be written as:

$$\sigma_{\mathrm{DR}}(E_{\mathrm{cm}}) = \frac{hg_d}{2k_e^2 g_i} \frac{\Gamma}{4(E_{\mathrm{cm}} - E_d)^2 + \Gamma^2} \times \frac{A_a(i \to d) \sum_f A_r(d \to f)}{\sum_k A_a(d \to k) + \sum_m A_r(d \to m)} \tag{12}$$

where k_e is the electron wave number, $\Gamma(d)$ is the total width of the resonance state, g_i and g_d are the statistical weights of the initial ionic core state (i) and the intermediate state (d), and A_a and A_r are the autoionizing and radiative decay rates. In the sums, f runs over all final states that are stable with respect to autoionization, k runs over all autoionizing decay channels of state d, and m includes all channels to states below d.

The integrated cross section, or resonance strength, is determined by the transition rate into the doubly excited state, i.e. the autoionization rate of the doubly excited state in the time reversed process, and the radiative branching ratio from this state to all states below the ionization threshold. The resonance strength will be governed by the rate of the weakest of these two channels: autoionization or radiative decay. For all the resolved resonances in the experimental data we found that the strengths are determined by the radiative decay rate. The theoretical calculations show that radiative stabilization of the "outer electron" is of considerable importance for the cross section.

A simplified picture of the DR rate dependence on the main quantum numbers and nuclear charge of the ion can be obtained by the following considerations. For high quantum states (Rydberg states n_2, l_2) the radiative rate A_r is independent of n, l and determined only by the core excited state n_1, l_1. The autoionization rate $A_a(n_2, l_2)$ varies with n_2^{-3}. For low n_2, l_2 one has $A_a \gg A_r$ and $\sigma_{\mathrm{DR}} \sim n_2^2$. Therefore, σ_{DR} for, e.g. the $(K\epsilon \to Ln_2)$ series should increase for low n_2 and start to decrease for higher n_2 ($\sigma_{\mathrm{DR}} \sim n_2^{-3}$). Because $A_r \sim Z^4$ this n dependence of the DR cross section varies with the ion nuclear charge.

Although the resonance strengths are determined by the radiative decay rate, it is $A_a(i \to d)$ that determines the positions of the resonances. This is seen nicely in Fig. 5, where DR $\Delta n = 0$ absolute recombination rates forming Ne^{6+} (middle) are compared with measurements of Auger spectra [56] for doubly excited states in Be-like Ne (top). The DR $\Delta n = 0$ transitions forming Be-like Ne correspond to Coster–Kronig transitions in the Auger spectra. The accuracy and resolution reached presently in recombination experiments are obviously superior and more crucial tests of calculations of the energies and resonance strengths are possible. An overview of the absolute rate coefficients calculated by the AUTOSTRUCTURE code is shown in the bottom part of the figure.

In this code the rate coefficient is calculated for single isolated DR resonances, i.e. their separation should be larger than the natural line width. The rate coefficients are obtained from the code in so-called binned cross sections: $\Delta\sigma_{\mathrm{DR}}(E_{\mathrm{cm}})$ where the cross section is averaged over an energy bin ΔE_{cm}. The bin size is chosen so narrow that σ_{DR} can be considered constant there. The AUTOSTRUCTURE code is based on the many-body Breit–Pauli approximation for the wavefunctions in intermediate coupling for low n and the high n states are obtained by extrapolating radial wavefunctions assuming quantum defect theory. Single resonances are not distinguished in the binned cross section representation. The DR rate coefficient $\alpha_{\mathrm{DR}}(E_{\mathrm{rel}})$ as a function of the relative longitudinal energy between electrons and ions is then obtained by folding $v_{\mathrm{cm}}\Delta\sigma_{\mathrm{DR}}(E_{\mathrm{cm}})$ over the electron velocity distribution. The agreement in the absolute rate coefficient between theory and experiment is

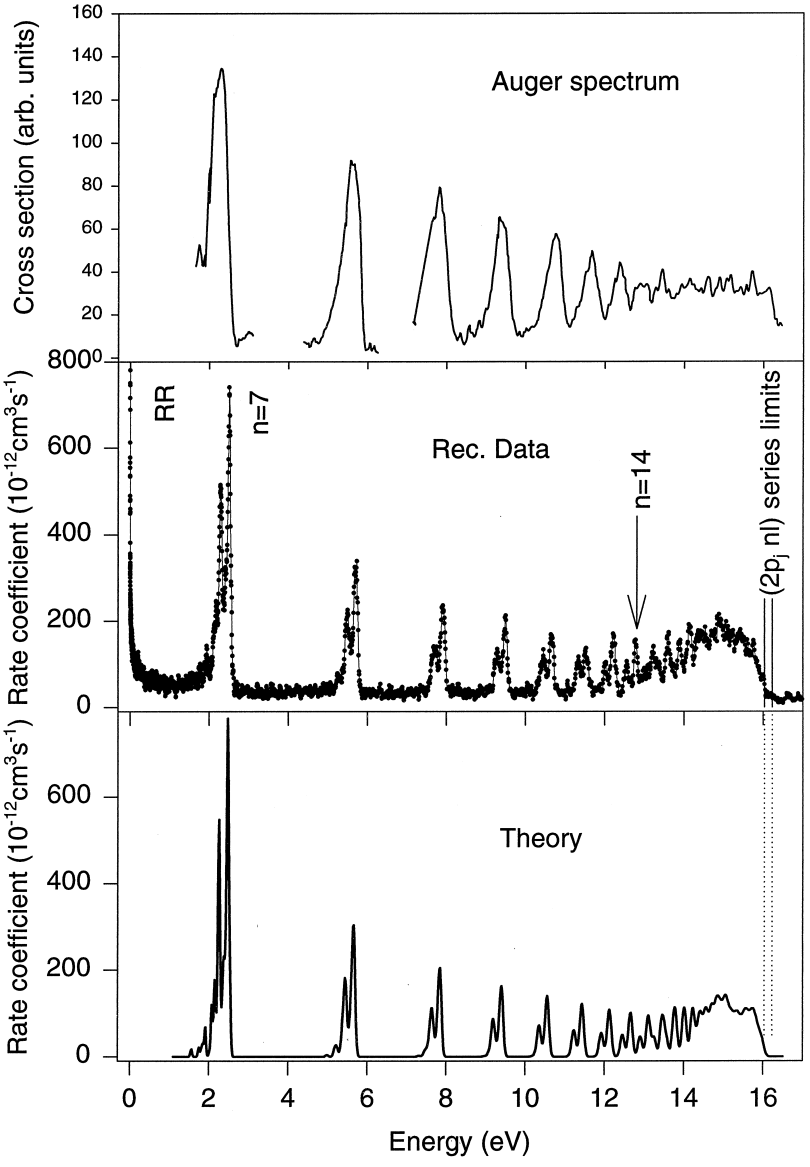

Fig. 5. Top: Auger spectra [56] for doubly excited states in Be-like Ne. Middle: DR $\Delta n = 0$ absolute recombination rates forming Ne^{6+}. The highest resonance that can be well identified is indicated. The double peaks are the resolved $2p_{1/2}nl$ and $2p_{3/2}nl$ resonance series. The sharp rate increase near zero energy (indicated as RR) is due to contributions of nonresonant recombinations (see Fig. 4). A calculation (see text) convolved with $kT_{\perp} = 10$ meV and $kT_{\parallel} = 0.13$ meV is shown in the lower part for comparison.

within 15 percent and thus within the experimental error bars.

The resolution achieved in Ne^{6+} DR resonances (Fig. 5 middle) is 10^{-2} eV full width at half maximum in the low energy region. The DR resonances in the figure have a double peak feature, corresponding to the excitations of the $2s$ core electron to $2p_{1/2}$ and $2p_{3/2}$ states. The first resonance peak corresponds to the free electron being captured to $n = 7$. From there on each $n_2 l_2$ resonance group can be clearly identified

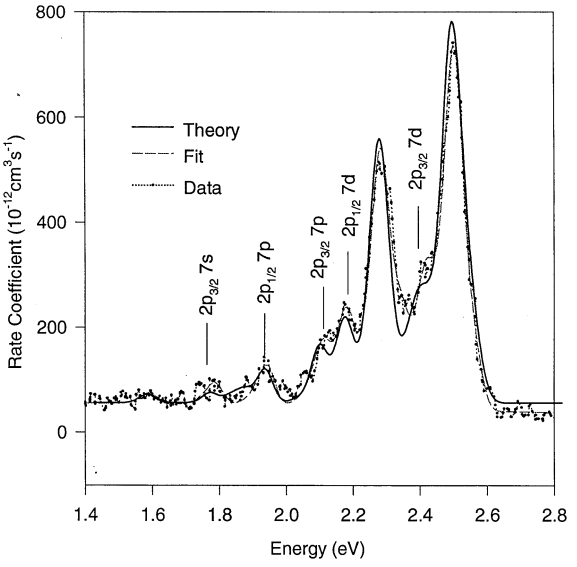

Fig. 6. Recombination rate coefficient for Ne^{7+} vs. relative energy for the $2p_{1/2}(7\ell)$ and $2p_{3/2}(7\ell)$ resonances only. The full line represents the calculated spectrum (folded with 10 meV/k_B transverse temperature and 0.13 meV/k_B longitudinal temperature). The angular momentum values of the highest electron are indicated.

up to $n = 14$ as indicated in Fig. 5. The absolute measured and calculated rates agree very well. On the high energy side, the resonances from $2p_j nl$ states of higher n overlap and accumulate to a bump at the series limit. Below we discuss the importance of radiative stabilization of Rydberg states for dielectronic recombination at the series limit at the examples of Ne^{7+} and Ar^{15+} ions.

The results for the lowest lying DR resonances with Ne^{6+} are displayed in Fig. 6. The theoretical cross sections from AUTOSTRUCTURE are folded with a distribution of electron beam temperatures $T_\perp = 10$ meV/k_B and $T_\parallel = 0.13$ meV/k_B. The calculation reproduces the shapes of all visible features in the data very well. However, an energy shift of 28 meV is needed to match the data. Uncertainties exist in the theoretical energy positions by contributions from quantum electrodynamical corrections, from the Breit interaction, and correlations in this order. As indicated in the figure, the resolved features are from DR via $1s^2 2p_{1/2}$ $7p$, $7d$ and $1s^2 2p_{3/2}$ $7s$, $7p$, $7d$ doubly excited states. The peaks of the low l states are clearly seen at the achieved resolution. States with higher l are not resolved and build up in two main peaks. The electron temperature as free parameters derived in the fit to these resonances are $kT_\perp = 30$ meV and $kT_\parallel = 0.13$ meV. The transverse temperature obtained by the fit to the DR resonance peaks is higher than the expected value of 10 meV. In order to see the significance of the fitted temperatures, we folded the calculation with different electron temperatures and compared the shape of the resulting curves with that of our data. The comparison shows that folding with $kT_\perp = 10$ meV and $kT_\parallel = 0.13$ meV also gives a good fit to the data. This phenomenon was also found in other experiments [20, 22]. One reason could be that the shape of DR resonances at around 1 eV are not very sensitive to the transverse temperature of 10^{-2} eV. Furthermore, the pronounced peaks may consist of multiple unsolved resonances of different J configurations. The energy spread of the resonances can broaden the width of the peaks, resulting in an apparently higher temperature, especially in the case where the statistical error is relatively large. Another possible reason is the neglect of the natural line width in our fit. Therefore the temperatures obtained by fitting DR peaks can only be regarded as an upper limit.

In order to get the $2p_{3/2} - 2p_{1/2}$ splitting from the data, the energy positions and resonance strengths of the resolved resonances high n and l are fitted with flattened Maxwell distributions. For states with an electron in high n and l the ion energy can be described by: $E_{\text{core}} + Z^{*2}\mathcal{R}/n^2$, where Z^* is the effective charge of the core. The resonance energy in a $\Delta n = 0$ DR transition from $1s^2 2s\ S_{1/2}$ to $1s^2 2p\ P_j nl$, $E_r(n)$, can thus be written as:

$$E_r(n) = \epsilon_j + \frac{Z^{*2}\mathcal{R}}{n^2} \tag{13}$$

where $\epsilon_j = E_{\text{core}}(1s^2 2p_j) - E_{\text{core}}(1s^2 2s)$, and $j = 1/2$ or $3/2$. We fit the measured resonance energies to such a formula with ϵ_j and Z^* as free parameters. The obtained values are $\epsilon_{1/2} = 16.029 \pm 0.008$ eV, $Z^* = 7.034 \pm 0.004$ for the $2p_{1/2}$ series and $\epsilon_{3/2} = 16.228 \pm 0.008$ eV, $Z^* = 7.026 \pm 0.004$ for the

$2p_{3/2}$ series. The deviation of all peaks are within 0.012 eV, which gives an estimate of the achieved precision. The $2p_{3/2} - 2p_{1/2}$ splitting derived from $\epsilon_{3/2} - \epsilon_{1/2}$ is 0.199 ± 0.011 eV. This value agrees with the result of 0.2045 eV obtained from a photon spectroscopic investigation [57].

In the calculated recombination rates at the Rydberg series limit, the fact that the ions pass through magnets and can be field ionized must be taken into account. The simplest approach is thus to truncate the sum over partial cross sections at the $n_{\max}$ (so called *hard* cutoff). However, a calculation using this simple approach does not agree very well with the experimental data. As shown in Fig. 5, a tail at the high energy side of the series limit is missing in the calculated rates. We therefore investigated cascading processes that can occur when the recombined ions travel from the cooler to the magnet. Recombined ions with $n_2 > n_{\max}$ can radiatively decay to states with $n < n_{\max}$ before reaching the magnet. They thus survive field ionization and reach the detector. To include this process, we have computed hydrogenic radiative decay rates for all possible electric dipole transitions for all populated Rydberg states. The dominant rates by far are those for the lowest-lying n allowed by the selection rules. Because $n_{\max}$ is much larger than the lowest-lying n, we only need to consider the first cascade step, and the radiative decay time to all states $n(<n_{\max})$ is equal to the total decay time to a very good approximation. Our dielectronic recombination cross sections to $1s^2 2pnl$ $(n > n_{\max})$ are then multiplied by the factor $1 - e^{-T_f/\tau(nl)}$ where T_f is the time of flight and the $\tau(nl)$ is the radiative decay time. We call this approach, which imposes an $n_{\max}$ after a time decay T_f, a "delayed cutoff."

In Fig. 7 calculations done for Ne^{6+} with a delayed $n_{\max} = 24$ and T_f equal to 5, 10, 20, 30 ns are displayed. The contribution of the high Rydberg states to the total cross section due to radiative decay to $n < n_{\max}$ states is counted up to $n_{\max} = 100$. In order to compare spectral shapes, the data has been divided by a factor of 1.2 and the energy scale of the calculation has been shifted by 120 meV to match the resolved resonance peaks. As shown in the figure the contribution of the high Rydberg states is clearly nonnegligible. The $T_f = 20$ ns curve exhibits best agreement with the data. The distance between the center of the cooler and dipole magnet is about 1.6 m and with the velocity of the ions (4.78×10^9 cm/s) this gives a flight time of $T_f \sim 30$ ns, which is quite close.

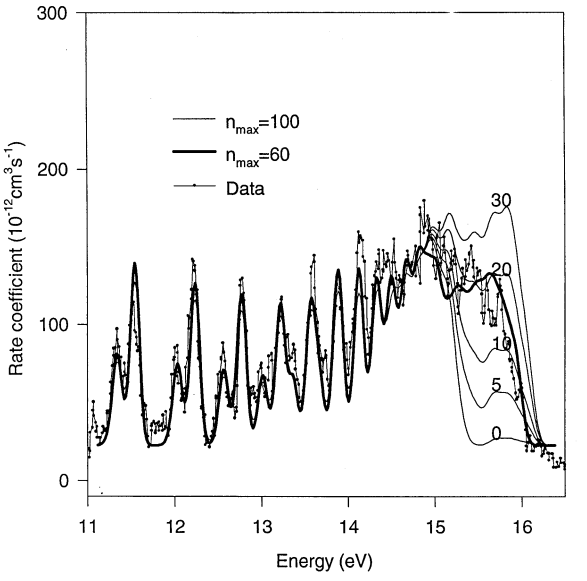

Fig. 7. Comparison of the rate coefficient in the region of high n states for Ne^{7+} with calculations employing different field cutoffs. Different delay times (see text) are indicated by numbers at the curves. The thick curve of $T_f = 20$ ns is calculated with an additional *hard* cutoff $n = 60$ due to the correction magnet.

In Fig. 8 the region of the high Rydberg states for Ar^{14+} in comparison with similar calculations is shown. At the energy of 11 MeV/u that this experiment was done, the hard cutoff is at $n_{\max} = 44$. The upper part in this figure shows the prediction of such a hard cutoff for this case. Considering a delayed cutoff with the delay times indicated in Fig. 8, the agreement is definitely improved. The flight time is similar to the Ne case, so a shorter delay time is also suggested by the Ar data.

In the calculations a field-free electron–ion interaction region is assumed. The presence of electric fields would enhance the dielectronic recombination rates [58]. It is due to mixing of ℓ in high n states that increases strongly the autoionization rates of those with high ℓ values. External electric fields can be caused by the motional field because of a transverse

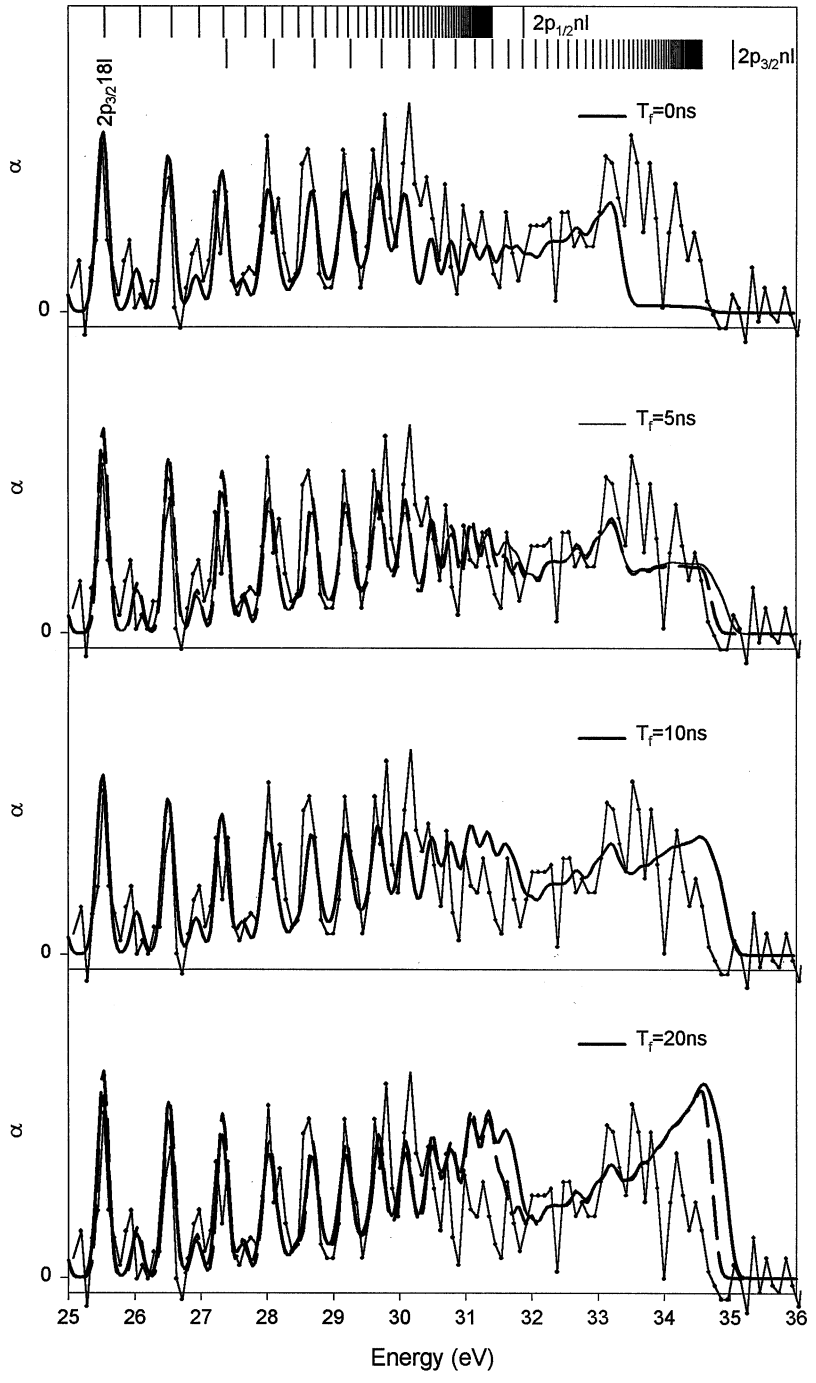

Fig. 8. Similar to Fig. 6 for Ar^{15+}. The dashed curves for $T_f = 5$ ns and $T_f = 20$ ns are calculated with an additional *hard* cutoff $n = 100$ due to the correction magnet.

solenoidial-magnetic field and by the space-charge field. These fields were minimized in the experiment by minimizing the angle between ion direction and solenoid-magnet field and by centering the ions in the electron-beam space-charge parabola. Still, small fields cannot be completely excluded. Thus the theoretical prediction is seen as a lower limit.

The discrepancy could suggest an underestimated decay times $\tau(nl)$ and/or an overestimated $n_{\max}$ because certain magnets in the flight path were not yet taken into account. In fact, there is a correction magnet near the cooler, thus two $n_{\max}$ and two T_f should be considered, T_{f-C}, $n_{\max-C}$ for the correction magnet and T_{f-B}, $n_{\max-B}$ for the bending magnet. Fortunately, with $T_{f-B} > T_{f-C}$ and $n_{\max-B} \ll n_{\max-C}$ it turns out that the effect of the correction magnet can easily be taken into account for all realistic values of T_{f-B} for Ne^{6+}, respectively Ar^{14+}. Those states with $n > n_{\max-C}$ are too long lived compared to T_{f-C} to avoid being field ionized. Thus, we model the whole evolution of the recombined states by a delayed cutoff as above and a hard cutoff $n_{\max-C} = 60$ and 100 for Ne^{6+} and Ar^{14+}, respectively. The results of this model are plotted in Fig. 8 by the dashed line and in Fig. 7 by the fat full line. It does fit the shape of the data better, especially at the high energy edge. However, it shows no dramatic difference in the height of the DR rate at high n. Including the effect of the correction magnet does not change the fact that the theory needs a shorter flight time for a good agreement with the data. This could be due to an underestimate of the decay time $\tau(nl)$, or an alteration of the l distribution of the recombined ion by the field and the simplifications in the delayed cutoff model. Detailed calculations considering the field distribution along the flight path, the l distribution of the recombined ions, and a more elaborate field ionization model are needed.

4. Conclusion

This report shows that storage rings, with expanded electron beams for cooling energetic ion beams, are very useful for electron ion recombination studies. For bare ions of up to charge 14 and certain Li-like ions, the experimentally observed rate coefficient is enhanced by up to a factor of 3 as compared to radiative recombination near zero relative energy. Dielectronic recombination resonances of Li-like Ne and Ar can be measured with an accuracy in the energy scale in the order of 10 meV. Energy positions and sizes of the cross sections are found in reasonable good agreement with the values calculated in an isolated resonance many-body Breit–Pauli approximation. Field stripping of recombination into high Rydberg states was considered in detail and shown that stabilization of these electrons on the flight path from the interaction region to the field region changes drastically the cross section.

Acknowledgement

This work was supported by the Swedish Natural Science Research Council (NFR).

References

[1] R. Schuch, in Review of Fundamental Processes and Applications of Atoms and Ions, C.D. Lin (Ed.), World Scientific, Singapore, 1993.
[2] F. Bosch, in Physics of Electronic and Atomic Collisions, T. Andersen, B. Fastrup (Eds.), AIP Conf. Proc., AIP, Woodbury, NY, 1993, p. 3.
[3] R.E. Marrs, P. Beiersdorfer, D. Schneider, Phys. Today October (1994) 27.
[4] M. Larsson, Rep. Prog. Phys. 58 (1995) 1267.
[5] R. Stensgaard, Phys. Scr. T22 (1988) 315.
[6] K. Abrahamsson, G. Andler, L. Bagge, E. Beebe, P. Carle, H. Danared, S. Egnell, K. Ehrnsten, M. Engstroem, C.J. Herrlander, J. Hilke, J. Jeansson, A. Kællberg, S. Leonstein, L. Liljeby, A. Nilsson, A. Paal, K.-G. Rensfelt, U. Rosengaard, A. Simonsson, A. Soltan, J. Starker, M. af Ugglas, A. Filevich, Nucl. Instrum. Methods B79 (1993) 269.
[7] K. Blasche, D. Bohne, B. Franzke, H. Prange, IEEE Trans. Nucl. Sci. NS-32 (1985) 2657, and B. Franzke, Nucl. Instrum. Methods Phys. Res. B 24/25 (1987) 18.
[8] T. Tanabe, K. Noda, T. Honma, M. Kodeira, K. Chida, T. Watanabe, N. Noda, S. Watanabe, A. Mizobuchi, M. Yoshizawa, T. Katayama, and H. Muto, Nucl. Instrum. Methods A 307 (1991) 7.
[9] P. Baumann, M. Blum, A. Friedrich, C. Geyer, M. Grieser, B. Holzer, E. Jaeschke, D. Kraemer, C. Martin, K. Matl, R.

Mayer, W. Ott, B. Povh, R. Repnow, M. Steck, E. Steffens, W. Arnold, Nucl. Instrum. Methods A 268 (1988) 531.
[10] See e.g. CERN Accelerator School, CERN 84-15, P. Bryant, S. Newman (Eds.), 1984, CERN 85-19, P. Bryant, S. Turner (Eds.), 1985, and CERN 87-03, S. Turner (Ed.), 1987.
[11] C.I. Budker, N.S. Dikansky, V.I. Kudelainen, I.N. Meshkov, V.V. Parkomchuk, D.V. Pestrikov, A.N. Skrinsky, B.N. Sukhina, Part. Accel. 7 (1976) 197.
[12] S. Schroeder, R. Klein, N. Boos, M. Gerhard, R. Grieser, G. Huber, A. Karafillis, M. Krieg, N. Schmidt, T. Kuehl, R. Neumann, A. Balykin, M. Grieser, D. Habs, E. Jaeschke, D. Kraemer, M. Kristensen, M. Music, W. Petrich, D. Schwalm, P. Sigray, M. Steck, B. Wanner, A. Wolf, Phys. Rev. Lett. 64 (1990) 737.
[13] H. Danared, et al., Phys. Rev. Lett. 72 (1994) 3775.
[14] A.V. Aleksandrov, N.S. Dikansky, N.Ch. Kot, V.I. Kudelainen, V.A. Lebedev, P.V. Logachov, Proceedings of the Workshop on Electron Cooling and New Cooling Techniques, Legnaro, Italy, 1990, p. 279.
[15] R. Schuch, T. Quinteros, M. Pajek, Y. Haruyama, H. Danared, H. Gao, G. Andler, D. Schneider, J. Starker, Nucl. Instrum. Methods Phys. Res. B 79 (1993) 59.
[16] F. Brouillard, in Atomic and Molecular Proceses in Controlled Thermonuclear Fusion, C.J. Joachain, D.E. Post (Eds.), Plenum, New York, 1983.
[17] H. Danared, Phys. Scr. 48 (1993) 405.
[18] W. Zong, R. Schuch, N. Badnell, Gao Hui, D.R. DeWitt, S. Asp, H. Danared, J. Phys. B 31 (1998) 3729.
[19] S. Asp, R. Schuch, D.R. DeWitt, C. Biedermann, Gao Hui, W. Zong, G. Andler, E. Justiniano, Nucl. Instrum. Methods B 117 (1996) 31.
[20] D.R. DeWitt, R. Schuch, Gao Hui, W. Zong, S. Asp, N. Badnell, M. Chen, Phys. Rev. A 53 (1996) 2327.
[21] R. Schuch, W. Zong, D.R. DeWitt, Gao Hui, S. Asp, J. Hvarfner, E. Lindroth, H. Danared, A. Källberg, Hyperfine Interact. 99 (1996) 317.
[22] W. Zong, R. Schuch, E. Lindroth, Gao Hui, D.R. DeWitt, S. Asp, H. Danared, Phys. Rev. A 56 (1997) 386.
[23] J. Dubau, S. Volonté, Rep. Prog. Phys. 43 (1980) 199.
[24] D.E. Osterbrock, Astrophysics of Gaseous Nebulae and Active Galactic Nuclei, Univ. Science Books, Mill Valley, CA, 1989.
[25] Y. Hahn, in Atomic and Molecular Processes in Fusion Edge Plasmas, R. Janev (Ed.), Plenum, New York, 1995, p. 91.
[26] A. Burgess, Astrophys. J. 139 (1964) 776; 141 (1965) 1588.
[27] W. Spies, A. Mueller, J. Linkemann, A. Frank, M. Wagner, C. Kozhuharov, B. Franzke, K. Beckert, F. Bosch, H. Eickhoff, M. Jung, O. Klepper, W. Koenig, P. Mokler, R. Moshammer, F. Nolden, U. Schaaf, P. Spädtke, M. Steck, P. Zimmerer, N. Gruen, W. Scheid, M.S. Pindzola, N.R. Badnell, Phys. Rev. Lett. 69 (1992) 2768.
[28] G. Kilgus, D. Habs, D. Schwalm, A. Wolf, R. Schuch, N.R. Badnell, Phys. Rev. A 47 (1993) 4859.
[29] D.R. DeWitt, R. Schuch, T. Quinteros, G. Hui, W. Zong, H. Danared, N. Badnell, Phys. Rev. A 50 (1994) 1257; and D.R. DeWitt, E. Lindroth, R. Schuch, Gao Hui, T. Quinteros, W. Zong, J. Phys. B 28 (1995) L147.
[30] H.T. Schmidt et al., Phys. Rev. Lett. 72 (1994) 1616.
[31] S. Mannervik, S. Asp, L. Brostrom, D.R. DeWitt, J. Lidberg, R. Schuch, Phys. Rev. A 55 (1997) 1810; and S. Mannervik, D.R. DeWitt, J. Lidberg, R. Schuch, Phys. Rev. Lett. 81 (1998) 313.
[32] H.A. Kramers, Philos. Mag. 46 (1923) 836.
[33] A. Burgess, Mon. Not. R. Acad. Soc. 118 (1958) 477.
[34] F.D. Aaron, A. Costescu, C. Dinu, J. Phys. 3 (1993) 1227.
[35] H.A. Bethe, E. Salpeter, Handb. Physik 35 (1957) 88.
[36] M. Stobbe, Ann. Physik 7 (1930) 661.
[37] M. Pajek, R. Schuch, Phys. Rev. A 45 (1992) 7894; Phys. Lett. A 166 235 (1992); Phys. Rev. A 46 (1992) 7334; and M. Pajek, R. Schuch, Nucl. Instrum. Methods B 93 (1994) 241.
[38] L.H. Andersen, J. Bolko, P. Kvistgaard, Phys. Rev. Lett. 64 (1990) 729.
[39] L.H. Andersen, J. Bolko, Phys. Rev. A 42 (1990) 1184.
[40] L.H. Andersen, J. Bolko, J. Phys. B 23 (1990) 3167.
[41] L.H. Andersen, G.-Y. Pan, H.T. Schmidt, 25 (1992) 277.
[42] H.T. Schmidt, G.-Y. Pan, L.H. Andersen, J. Phys. B 25 (1992) 3165.
[43] A. Wolf, J. Berger, M. Bock, D. Habs, B. Hochadel, G. Kilgus, G. Neureither, U. Schramm, D. Schwalm, E. Szmola, A. Müller, M. Wagner, R. Schuch, Z. Phys. D 21 (1991) S69.
[44] A. Müller, S. Schennach, M. Wagner, J. Haselbauer, O. Uwira, W. Spies, E. Jennewein, R. Becker, M. Kleinod, U. Pröbstel, N. Angert, J. Klabunde, P.H. Mokler, P. Spädke, B. Wolf, Phys. Scr. T37 (1991) 62.
[45] A. Frank, A. Müller, J. Haselbauer, S. Schennach, W. Spies, O. Uwira, M. Wagner, R. Becker, M. Kleinod, E. Jennewein, N. Angert, P.H. Mokler, AIP Conference Proceedings 274: Manhattan, 1992, P. Richard, M. Stökli, C.L. Cocke, C.D. Lin (Eds.), New York, 1992, p. 532.
[46] D.R. Bates, et al., Proc. R. Soc. A 267 (1962) 297.
[47] Gao Hui, D.R. DeWitt, R. Schuch, W. Zong, S. Asp, M. Pajek, Phys. Rev. Lett. 75 (1995) 4381.
[48] Gao Hui, R. Schuch, E. Justiniano, D.R. DeWitt, W. Zong, W. Spies, H. Lebius, J. Phys. B Lett. 30 (1997) L1.
[49] T. Quinteros, Gao Hui, D. DeWitt, R. Schuch, M. Pajek, S. Asp, Dz. Belkic, Phys. Rev. A 51 (1995) 1340.
[50] Gao Hui, E. Justiniano, S. Asp, D.R. DeWitt, H. Danared, R. Schuch, Phys. Rev. A 54 (1996) 3005.
[51] R. Schuch, T. Quinteros, M. Pajek, Y. Haruyama, H. Danared, Gao Hui, G. Andler, D. Schneider, J. Starker, Nucl. Instrum. Methods B 79 (1993) 59; and R. Schuch, Dz. Belkic, E. Justiniano, W. Zong, Gao Hui, Hyperfine Interact. 108 (1997) 195.
[52] C. Biedermann, Gao Hui, R. Schuch, W. Zong, S. Asp, D.R. DeWitt, H. Kuiper, J. Phys. B 28 (1995) 505.
[53] Gao Hui, D.R. DeWitt, R. Schuch, W. Zong, S. Asp, M. Pajek, Hyperfine Interact. 99 (1996) 301.
[54] M. Pajek, R. Schuch, Hyperfine Interact. 108 (1997) 185.
[55] C.E. Theodosiou, M. Inokuti, S. Manson, At. Data Nucl. Data Tables 35 (1986) 473.
[56] N. Stolterfoht, Phys. Rep. 146 (1987) 317.
[57] K.G. Winding, J.D. Purcell, Astrophys. J. 204 (1976) L151.
[58] T. Bartsch, A. Müller, W. Spies, J. Linkemann, H. Danared, D.R. DeWitt, H. Gao, W. Zong, R. Schuch, A. Wolf, G.H. Dunn, M. Pindzola, D. Griffin, Phys. Rev. Lett. 79 (1997) 2233.